Cytometry 17:1–12 (1994)

Automatic Detection of Clustered, Fluorescent-Stained Nuclei by Digital Image-Based Cytometry[1]

Stephen J. Lockett[2] and Brian Herman

Lawrence-Berkeley Laboratory, Berkeley, California 94720 (S.J.L.) and Laboratories for Cell Biology, Department of Cell Biology and Anatomy, University of North Carolina, Chapel Hill, North Carolina 27599–7090 (B.H.)

Received for publication December 15, 1993; accepted April 15, 1994

Automatic image-based cytometry (IC) can conveniently quantify the distributions of several specific, fluorescence-labeled molecules within individual, isolated cells of slide- or tissue-based specimens. However, many specimens contain clusters of cells or nuclei that are not detected as individual entities by existing automatic methods. We have developed analysis algorithms which detect individual nuclei occurring in clusters or as isolated nuclei. Specimens were labeled with a fluorescent DNA stain, imaged and the images were segmented into regions of nuclei and background. Clusters of nuclei, identified by their size and shape, were divided into individual nuclei by searching for dividing paths between nuclei. The paths, which need not be straight, possessed the highest average gradient per pixel. In addition, both high- and low-pass filtered images of the original image were analyzed. For each individual nucleus, one of the three segmented regions representing the nucleus (from either the original or one of two filtered images) was chosen as the final result, based on the closeness of the regions to average nuclear morphology. The algorithms correctly detected a high proportion of isolated (328/333) and clustered (254/271) nuclei when applied to images of 2 μm prostate and breast cancer sections. Thus, these algorithms should enable much more accurate detection and analyses of nuclei in intact specimens.

Key terms: Image analysis, image cytom etry, nuclei, tissue sections

Digital image-based cytometry (IC) is a technique which analyses slide-based specimens using a microscope coupled to an electronic camera and computer. The images are stored digitally in computer memory from where they are accessible for analysis by software algorithms. IC is now a primary technique for understanding normal and pathological cellular mechanisms, because it is possible to quantitatively and nondestructively measure wide ranges of biochemical, morphological, densitometric, and contextual parameters on the individual cells and nuclei in the specimens (2,10,21,23,24,25,29,38,40).

The convenient measurement of many individual nuclei requires image analysis algorithms that automatically locate every nucleus. This is usually accomplished by staining the nuclei in such a way that their corresponding image intensities are significantly different from the background intensities. Then, an algorithm that calculates threshold intensities between nuclear and background intensities, can be used to segment the nuclei from the background (26). In our IC (10,24), specimens are stained with a fluorescent DNA dye, because all nuclei contain abundant DNA and are thus represented in the images by high pixel intensities against a low intensity background. Images are automatically segmented into regions representing nuclei and background. This method, and others (27), correctly detects almost 100% of isolated nuclei (24).

In most specimens, particularly clinical specimens, there are clustered cells where different nuclei appear touching or overlapping in the images. Consequently, large intensity differences no longer exist between the nuclei and such clusters can thus be mistakenly de-

[1]Supported by a Biomedical Engineering research grant from the Whitaker Foundation and the Department of Energy contract DE-AC03–76-SF00098.

[2]Address reprint requests to Stephen J. Lockett, Mail-stop 74–157, Lawrence-Berkeley Laboratory, 1 Cyclotron Road, Berkeley, CA 94720.

tected as a single nucleus. Despite many attempts to devise algorithms that recognize individual nuclei within clusters, none have proven satisfactory for wide biological or clinical application. Some workers (1,9, 31,33,36) have reported over 90% (and often over 95%) of nuclei being correctly segmented, but in these studies: (1) most nuclei in their images were isolated; (2) the analysis was limited to only isolated nuclei or nuclei which appeared to barely touch in the images, or (3) the proportion of clustered nuclei in the images was not reported. When segmentation techniques were deliberately applied to clustered nuclei, lower success rates have been reported. For example, Bartels et al. (3,4) described the automatic segmentation of 4 μm Feulgen-stained sections of prostatic carcinoma, where the proportion of clustered nuclei was high based on the published images. They correctly segmented over 90% of the nuclei in 64% of the fields and over 80% in another 24% of the fields (6). Garbay et al. (11) segmented images of 150 erythrocytes appearing to overlap in May-Grünwald-Giemsa stained smears of bone marrow cells and correctly segmented 79% of them.

The reason why clustered nuclei are not correctly segmented is unknown, but may be partly due to the fact that most methods do not utilize all the information contained in the images. For example, some methods use only morphological information derived from binary masks of clusters (9,31,41,42), and consequently do not use pixel intensity information. Other methods use both morphological and intensity information, but alternate their use (1,11,37). Gray-scale morphology operations (30) simultaneously utilize both morphological and intensity information and thus show promise, but they have not yet been extensively applied to segmenting clustered nuclei.

The aim of this study was to develop algorithms that would correctly detect at least 90% of the individual nuclei in specimens containing large proportions of clustered nuclei. To achieve this aim, the algorithms were designed with the following properties: (1) simultaneous use of both morphological and intensity information; (2) utilization of a priori knowledge about the size and shape of nuclei (22); (3) insensitivity to minor changes in system parameters; (4) low sensitivity to noise expressed as pixel intensity variations; (5) not restricted to particular types of specimens or classes of clustered nuclei (e.g., only nuclei that appeared to barely touch in the images), and (6) the ability to identify a subset of nuclei with a higher probability (much more than 90%) of being correctly detected relative to the other (detected) nuclei.

Images of Hoechst-stained epithelial nuclei in 2 μm sections from prostate and breast tumors were used to test the algorithms, because: (1) breast and prostate cancer are respectively the third and forth most common cancers in the United States (19); (2) the present method of grading (visual examination of the epithelial cells in the sections) would benefit from a more objective classification of the morphology and distribution of the epithelial nuclei (6); (3) these sections contain large proportions of closely spaced epithelial cells (20) that appear to touch in the images, and (4) the cells that appear to touch are in the same focal plane. Therefore their analysis will probably not be significantly improved by using three-dimensional (3D) imaging, because such imaging mainly improves the resolution of signals between different focal planes.

MATERIALS AND METHODS

Image Analysis Procedure

Overview Figure 1A summarizes the image analysis procedure and Figure 1B defines the terms (underlined in Fig. 1B) used below. Referring to Figure 1A, each original image of fluorescent stained nuclei was both high-pass and low-pass filtered to produce versions with enhanced and suppressed edge information, respectively. Enhancing the edges increased the likelihood that the segmentation algorithm would find the edges between (clustered) nuclei. However, enhancement also increased the likelihood that false edges within individual nuclei would be detected and incorrectly used to divide the cluster. Suppressing the edges had an opposite effect on the segmentation.

The original image and both filtered versions were analyzed by the segmentation algorithm. This algorithm automatically calculated threshold intensities to segment the images into regions (which consisted of 4-connected pixels) representing stained nuclei and background. Size and shape parameters were used to differentiate regions corresponding to clustered vs. isolated nuclei. Finally, the algorithm attempted to divide each region of clustered nuclei into new regions representing individual nuclei.

The input to the decision algorithm were the regions representing individual nuclei in the segmented images of the original and high- and low-pass filtered original image. The decision algorithm first assigned regions, which were in the same location in the three segmented images, to the same group. Then, taking each group individually, the set of regions from the same version of the image, which was collectively closest to the average size and shape of nuclei, were chosen as the final segmented individual nuclear regions for the original image.

The benefit of filtering the original image before segmentation and combining the results from the original image and filtered versions after segmentation is as follows. Incorrectly divided nuclei in the original image (for example, because of the existence of a false edge), would not be identified as such in the segmented low-pass filtered version (because false edges would be suppressed). Consequently, the decision algorithm would probably choose the (correct) region from the low-pass version, because it would be closer to an average nucleus than the two (incorrect) regions in the segmented versions of the original and high-pass filtered images. Conversely, the segmentation might fail to divide a cluster of two nuclei in the original image (because of a

weak edge between them), but would successfully divide the cluster in the high-pass version (because the edge would be enhanced). In this situation, the decision algorithm would probably choose the correct regions from the high-pass version.

Image filtering. The images were low-pass filtered by two successive applications of an averaging filter (13) with a kernel size of 11 × 11 pixels. The high-pass filtering was done by halving the pixel intensities of the low-pass version and subtracting the resulting image from the original image. These filters were empirically selected, based on the final results when analyzing a subset of representative images.

Image thresholding. The segmentation algorithm first calculated threshold intensities (described in reference 24) to divide the images into regions corresponding to nuclei and background. The output from thresholding was another image, where background pixels had intensities (henceforth named "values") of 255 and nuclear pixels had values ≠ 255. All pixels in the same contiguous region had the same value, but pixels in different regions had different values.

Cluster detection. Cluster detection used a priori knowledge about nuclei to recognize regions corresponding to clustered nuclei. Such regions had larger areas (measured in pixels) and more irregular shapes (measured by the shape factor, SF) than individual nuclei. SF was defined as perimeter^2/area, where the perimeter was taken as the number of pixels around the edge of the region. Any region was treated as a cluster if it had either an area and an SF more than the mean area of individual nuclei (*AREA*) and 15.5, respectively, or an area more than 2 × *AREA*. These particular rules were empirically chosen because, based on visual examination of the images, they detected virtually all clusters and only a small proportion of single nuclei. Properties of the division algorithm (described below) ensured that most of these single nuclei were not divided.

Cluster division The division algorithm found dividing paths across clusters. A dividing path was defined as, "the path that possessed an average gradient (15) per pixel greater than all other possible paths," because the part of a cluster where two nuclei appear to overlap or touch would contain an increased proportion of nuclear edges either within the overlapping part or around its edges. Consequently, their corresponding pixels, on average, would have higher gradients than pixels inside the non-overlapping parts of the nuclei.

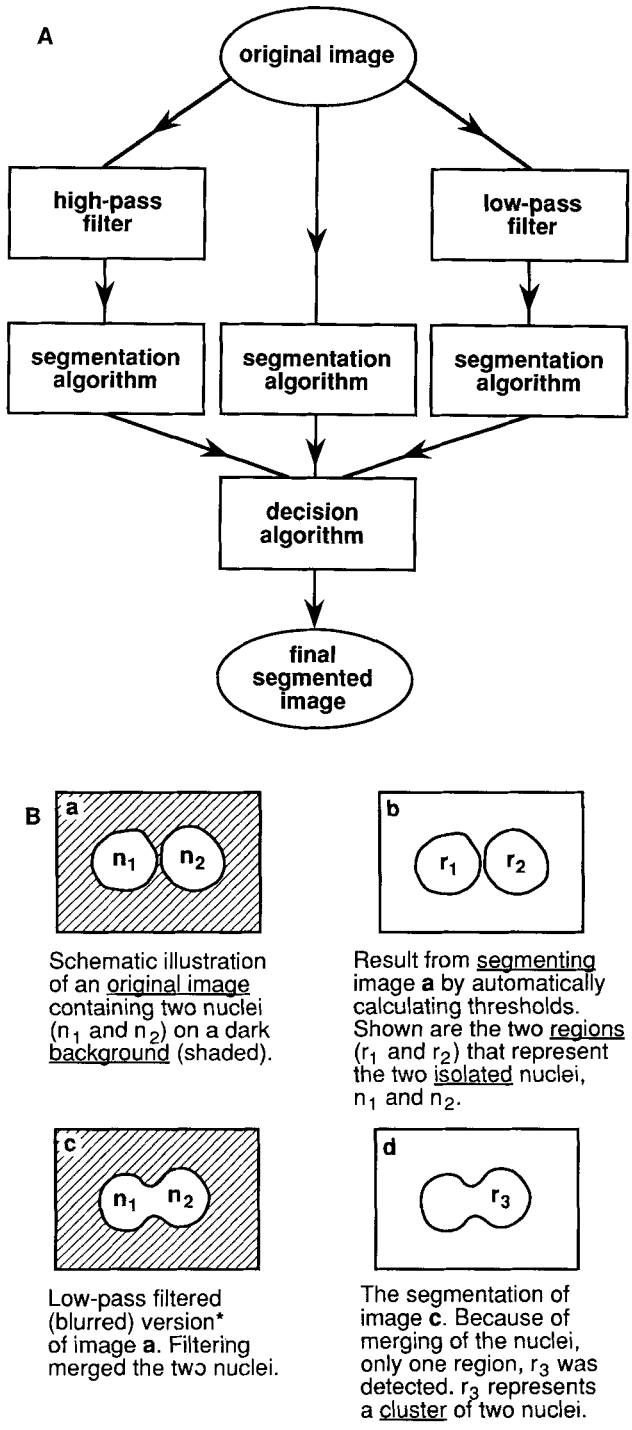

FIG. 1.

FIG. 1. **A:** The image analysis procedures illustrated as a flow diagram. The original image is both high-pass and low-pass filtered. The (same) segmentation algorithm is applied to the original image and both filtered versions. The decision algorithm takes as input the three results from the segmentations and outputs the final segmented image. **B:** Definition of the terms used (underlined) for describing the image analysis procedure. Refer to Figures 5, 6, and 7 for examples of real images and results from their analysis.

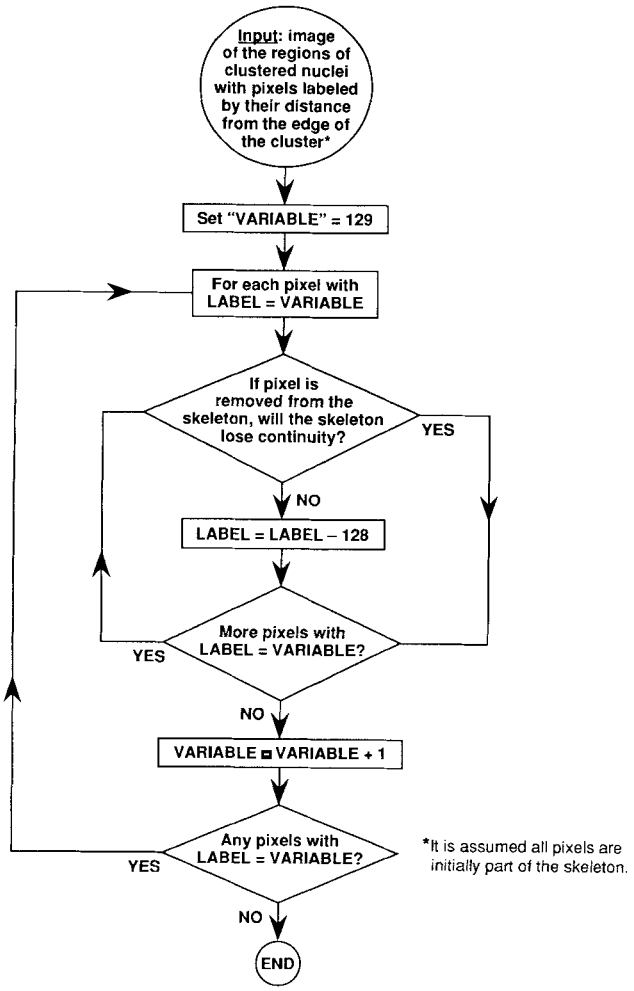

FIG. 2. Flow diagram of the algorithm used for determining the skeleton of a cluster.

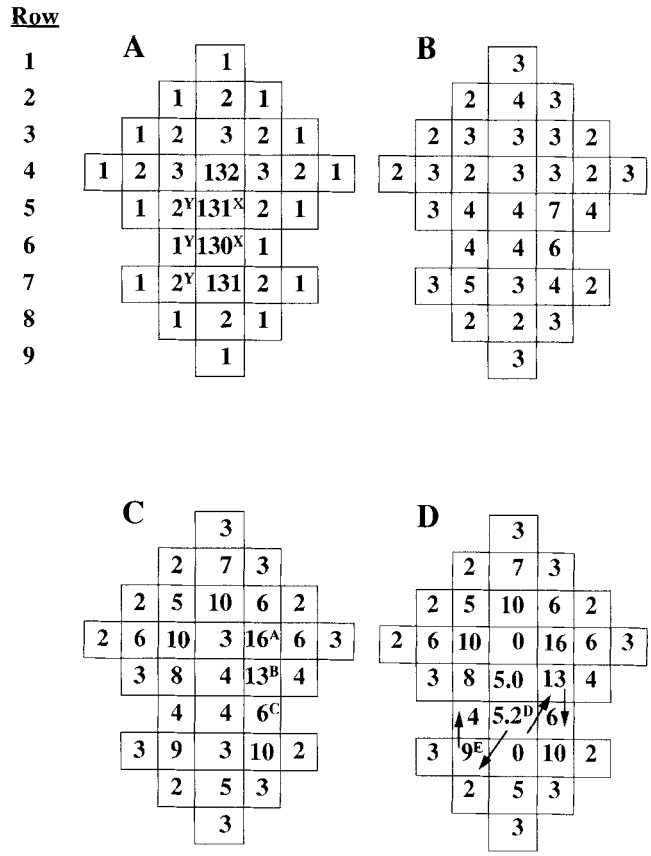

FIG. 3. **A:** A schematic cluster of two nuclei showing the labels assigned to the pixels using the algorithm described in Figure 2. Note that 128 is added to the labels of skeleton pixels. The pixels marked "X" are those through which a dividing path was allowed to pass. The pixels marked "Y" are on the left side of the skeleton and adjacent to the skeleton pixel labeled 130. **B:** The schematic cluster showing arbitrary gradients for each pixel. **C:** The result from applying the procedure for finding the "summed gradients" of the non-skeleton pixels. **D:** The result from applying the procedure for finding the best dividing path starting from each skeleton pixel. Each skeleton pixel now has its average gradient value. The two pixels at the ends of the skeleton have been assigned average gradient values of 0. The pixel marked "D" is the skeleton pixel with the largest average gradient value (5.2) and therefore lies on the dividing path. The pixel marked "E" has the highest average gradient out of the ones marked "Y" in A. The arrows show the actual dividing path.

Furthermore, a valid path was allowed to cross the skeleton (medial axis) (17) of the cluster only once, and on either side of the skeleton had to proceed towards the boundary of the cluster. This was because the skeleton generally ran between the centers of nuclei and thus the dividing path should be roughly orthogonal to it. Paths were 8-connected lines of pixels, but were not restricted to being straight lines.

Determination of the skeletons of clusters employed a standard method (16). First, each pixel in the cluster was given a label *approximately* equal to its shortest distance from the boundary of the cluster plus 128. This was done by assigning a label of 129 to pixels that were 4-connected to pixels outside the cluster and then assigning a label of 130 to pixels next to pixels with 129 labels, etc. Next, the skeleton was determined as described in Figure 2. Figure 3A shows a schematic example of a cluster of two nuclei labeled in this way.

The determination of the dividing paths was similar, in principle, to the grey-weighted distance transform (35), and was implemented as follows. First, the magnitude of the gradient of every pixel in the cluster was calculated by filtering the image with the 3 × 3 Sobel operator (14). Then, for each pixel with label 2 (see Fig. 3A), the algorithm located all pixels in the 8-connected surrounding pixels labeled 1. The highest gradient amongst the located pixels was chosen, and this gradient was added to the gradient of the pixel labeled 2. After applying the procedure to every pixel labeled 2, it was applied to every pixel labeled 3 using surrounding pixels labeled 2. The process continued until all pixels in the cluster, except those on the skeleton, had been covered. The resulting values for the pixels are called "summed gradients" and Figure 3C shows the result of

applying this procedure to the schematic cluster with the arbitrary gradients shown in Figure 3B. The result from this procedure enabled the best dividing path to be found from any non-skeleton pixel to the boundary of the cluster as follows. Starting from pixel "A" (arbitrarily chosen) in Figure 3C, the neighboring pixel which has the highest "summed gradient" and has a label less than the starting pixel (A) is found. This is pixel "B." The process is repeated from "B" until a boundary pixel is reached (pixel "C").

The next step found the best dividing path starting from every skeleton pixel, which had two neighbors (in an 8-connected surround) that were also skeleton pixels (i.e., the pixels marked "X" in Fig. 3A). For each of these valid skeleton pixels, the adjacent, non-skeleton pixels on one side of the skeleton were identified. (For example the pixels marked "Y" in Fig. 3A are on the left side of the skeleton and adjacent to the pixel labeled 130). For each of these non-skeleton pixels, its "summed gradient" was divided by its label to obtain its "average gradient." The pixel with the largest average gradient was noted and its summed gradient was added to the gradient of the skeleton pixel. (For example for the skeleton pixel labeled 130 in Fig. 3A, the pixel marked "E" in Fig. 3D has the largest average gradient out of the pixels marked "Y" in Fig. 3A.) Then, the procedure was repeated for the non-skeleton pixels on the other side of the skeleton. The result obtained for the skeleton pixel under consideration was its summed gradient and this number was divided by the lowest number of pixels across the cluster at this pixel to give its average gradient. Mathematically, this is: $\Sigma_i(G_i/N)$, where G_i are the magnitudes of the gradients of pixels, i, N is the number of pixels in the best dividing path ($= 2 \times$ [label of skeleton pixel $- 129$] + 1) and the summation is over the pixels in the best path. The procedure was repeated for all other valid skeleton pixels. (The numbers of 5.0 and 5.2 in Fig. 3D are the average gradients for the two valid skeleton pixels marked "X" in Fig. 3A.) For non-valid skeleton pixels (i.e., those at the end of the skeleton or where the skeleton splits), the average gradient was set to zero (see Fig. 3D).

The dividing path was restricted as to where it crossed the cluster, in order to further increase the chance that it followed the junction between two nuclei. In most clusters, such junctions corresponded to "necks" in the cluster (e.g., row 6 in Fig. 3A). Therefore, to bias the dividing path into these "necks," the place where the path crossed the skeleton line was restricted as follows: The skeleton pixel with the largest label was located (i.e., 132 at row 4 in Fig. 3A). The algorithm first moved along the skeleton line, starting at this pixel, for a distance equal to [label -128]/2 (i.e., two pixels for the cluster in Fig. 3). Then, the algorithm moved a second time along the skeleton line in the same direction up to a maximum distance equal to this largest label minus 128 (i.e., four pixels for the cluster in Fig. 3). During the second move, the skeleton pixel encountered with the largest, average gradient was taken as being on the dividing line (i.e., the pixel with value 5.2 in Fig. 3D). The remainder of the dividing path from this pixel to the cluster boundaries was found as described in the third paragraph of this subsection. The path was not allowed to travel along the skeleton. (The arrows in Fig. 3D show the path taken for that cluster.)

If, during either move along the skeleton, a pixel with average gradient equal to zero was encountered, then the algorithm terminated the search. If this occurred in the first move, then the cluster would not be divided on this attempt. In this situation, the search for the start of a different path was undertaken. Searching ended either with the cluster never being divided, or when a dividing path was found.

When a dividing path was found, the two new regions were reclassified as described in the section "Cluster detection." Then cluster division was repeated for those new regions classified as being clusters. This iterative procedure enabled large clusters of cells to be divided, by successively dividing larger clusters into smaller clusters until the smaller clusters consisted of two nuclei. The final round of the iteration would divide the clusters of two nuclei into individual nuclei.

The decision algorithm The regions detected from the original image and two filtered versions by the above analysis were the inputs to the decision algorithm (Fig. 1A). This algorithm first reduced the size of regions by successive morphological erosions for two purposes: (1) to remove regions too small to represent nuclei, and (2) to increase, in parts of the images containing many clustered nuclei, the combinations of regions this algorithm could choose between for the final results. The latter is explained below.

The next step in the algorithm assigned regions which overlapped (i.e., from different images) to the same group. The terms used below are defined in Figure 1B. Figure 4A shows schematically two nuclei, A and B segmented from the original image (regions A_1 and B_1) and a filtered version (regions A_2 and B_2). (The vertical dashed lines in Fig. 4 are only for visual alignment.) The actual decision algorithm used both filtered versions, but only one is used in this explanation for simplicity. Let us assume regions A_1 and B_2 are correctly segmented, but B_1 and A_2 are not. The decision algorithm assigns overlapping regions to the same group, thus all four regions are in the same group. This is because A_1 overlaps both A_2 and B_2, and B_2 overlaps B_1. The algorithm then chooses one of the sets of regions in the group as being the final result. Consequently, it would either choose the set (A_1, B_1), or (A_2, B_2). However, both choices would lead to a mistake, because either region B_1 or A_2 would be selected. Figure 4B shows the same region as Figure 4A after morphological erosions. Erosions were repeatedly applied with a 3×3 kernel and alternating between 8- and 4-connectedness. The *number of erosions* applied re-

duced the area of an average nucleus (= *AREA*) to 0.75 × *AREA*. The decision algorithm would now assign regions A_1 and A_2 to one group and regions B_1 and B_2 to another group, because neither A overlaps neither B or vice versa. Consequently, the algorithm may choose any combination of A's or B's, because each region is its own set. Most likely, regions A_1 and B_2 would be chosen because they are closer to the average size and shape of nuclei compared to regions B_1 and A_2. Hence the results from this step of the algorithm were that each group consisted of three sets, with each set containing the regions originating from the original image or one of its two filtered versions. Then for each group, the algorithm measured the closeness of each set to average nuclei. The closeness was defined as the (log) likelihood (32) that the regions in a given set were average nuclei and was measured using the equation:

$$L = 1/N \; X \sum_{n=1}^{N} \{(A_n - m_A)^2/\sigma_A{}^2 + (S_n - m_S)^2/\sigma_S{}^2\} \text{ for } N > 0 \;\Big|\; 0 \text{ for } N = 0 \;\Big| \quad \ldots(1),$$

where L is the (log) likelihood; N, the number of regions in the set under consideration; A_n, the area of region n; m_A, the mean area of nuclei; σ_A, the standard deviation of m_A; S_n, the shape factor of region n; m_S, the mean shape factor of nuclei; σ_S, the standard deviation of m_S. Hence, the closer a set of regions was to the mean area and mean shape factor of nuclei, the greater the likelihood. The likelihood measure assumed that the area and shape factor distributions for nuclei were Gaussian, and that the shape factor and area for a region were independent. Although, both assumptions were probably not accurate, the resulting likelihood measure was adequate for correctly selecting between the three sets in each group.

On occasions, nuclei detected from some versions of the image were missed in others and consequently some of the resulting sets would be missing regions. Although these sets are incorrect, their likelihood values could easily be greater than other sets containing all the regions. This would result in the set with missing regions being incorrectly selected. To avoid this situation, any set was chosen over another, if its total region area was greater than the total region area plus m_A of the other, regardless of likelihood values.

After final selection of the regions representing nuclei, the regions were dilated, using the reverse process to the erosions defined above, in order to return the regions to their original sizes following thresholding. Finally, regions considered too small, too large, too irregular (SF > 17) or on the edges of images were rejected.

Applications of the Image Analysis Procedures to Clinical Specimens

Specimen preparation. Biopsy material from prostate and breast cancer patients was fixed in 10% buffered formalin (pH 7.4) and then embedded in purified glycol methacrylate (5) (pH 7.4). The embedded material was sectioned with a glass knife 2 μm thick using a JB-4A microtome (Energy Beam Sciences, Inc., Agawam, MA). The sections were placed on glass slides and dried on a hot plate (50–60°C, 1 min.). The sections were labeled with the fluorescent DNA dye Hoechst 33342 (Molecular Probes, Eugene, OR) dissolved in phosphate buffered saline (PBS) (0.1 μg/ml, pH 7.4, 10 min, 20°C), followed by washing in PBS. A small drop of PBS, followed by a #1 coverslip, was placed over each section and the coverslip was sealed to the slide with non-fluorescent nail enamel.

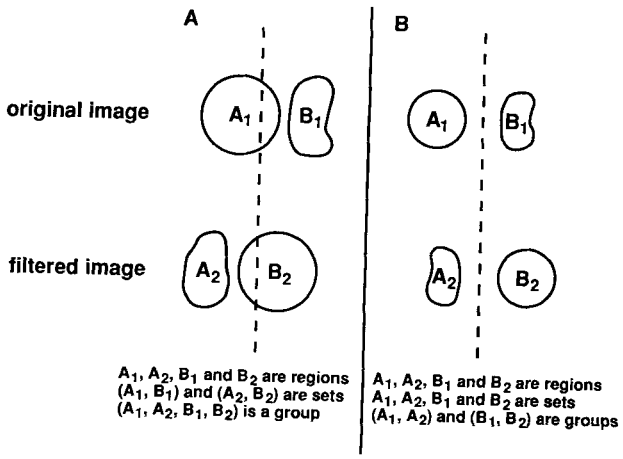

FIG. 4. Assignment of the detected regions to groups. The terms used below are defined in Figure 1B, but see the text for full explanation of this figure. (The vertical dashed lines are for visual alignment.) The sentences at the bottom of (A) and (B) are the results from application of the decision algorithm to these schematic nuclei. **A:** Schematic showing two nuclei, A and B segmented from the original image (regions A_1 and B_1) and a filtered version (regions A_2 and B_2). **B:** The same regions illustrated in A, but after morphological erosion.

Image acquisition. The images were acquired using an inverted epi-fluorescence microscope (Axiovert 10, Zeiss, Thornwood, NY) equipped with a filter cube, 40X dry objective lens (Plan-Neofluar, 0.75 numerical aperture, #40 03 50, Zeiss) and a Micro-Imager 1400 digital camera (Xillix Technologies Corp., Vancouver, Canada). The filter cube transmitted excitation light at 365 nm, had a dichroic mirror at 390 nm transition wavelength, and collected emitted fluorescence light above 410 nm. The camera images were 1,280 × 1,024 pixels with the intensity at each pixel digitized to 12-bits and mapped into 8-bits. They were acquired into an image-1280 board (Matrox Electronic Systems, Ltd., Dorval, Québec, Canada) on the back plane of an IBM compatible 486 personal computer (Gateway 2000, Des Moines, IA) and were subsequently transferred via ethernet to a SPARC-1 workstation (Sun Microsystems, Inc., Mountain View, CA) for archiving on optical disks.

Microscopic scenes, containing relatively large numbers of epithelial cells, were imaged. The camera exposure time was 200 msec and each pixel represented

0.16 × 0.16 μm of the section. Six images from a prostate specimen, one image from another prostate specimen, and one image from a breast specimen were acquired.

Image and data analysis. The images were divided into small images of 256 × 256 pixels, because some of the algorithms only handled that size. These small images overlapped each other by at least one average nucleus diameter so that any nucleus on the edge of one image was fully represented in the adjacent image.

First, a few small images were analyzed using the segmentation algorithms described in the sections Image thresholding, Cluster detection, and Cluster division, and using an approximate value for *AREA*. The output images, which consisted of regions representing nuclei, were eroded (see above for details) and then the area and perimeter of the first 20 correctly segmented individual nuclei (based on visual comparison to the original images) were measured. These data were used to determine *AREA*, m_A, σ_A, m_S, and σ_S. Next, all the small images were analyzed as described in the section Image Analysis Procedure, and the output images were then manually tiled into a 1,280 × 1,024 size image using the interactive tools provided by the Matrox imaging system. A nucleus located in the overlapping border regions of the small images were segmented more than once and thus there was more than one region representing it. The region furthest from the edge of its image was taken as the result, because this would minimize any edge effects. An inherent problem with thin sections was that nuclei were randomly cut (7). Therefore, the proportion of each nucleus present in the section continuously varied from zero up to a maximum; the maximum being where the section passed centrally through the nucleus. Consequently, an arbitrary lower limit had to be set on the size of detected nuclei, which was *AREA*/4.

The performance of the analysis was measured by calculating the fraction of isolated nuclei and the fraction of clustered nuclei correctly detected. Correctly and incorrectly detected nuclei were determined by visually comparing the acquired images to the images showing the regions determined by the analysis. Isolated nuclei were those correctly detected by only thresholding the original image. Clustered nuclei were those in the same region as at least one other nucleus after thresholding. A nucleus was considered correctly detected if its segmented region visually matched the shape of the nucleus in the original image. An overall performance measure was defined using the following expression:

$$\text{Performance} = (D - \text{ART})/V \quad (2),$$

where D was the number of correctly detected nuclei, ART(ifacts) was the number of regions not considered to be nuclei, and V was the number of nuclei visually counted in the original images.

RESULTS

The execution time of the algorithms for a small (256 × 256 pixels) image was around 30 sec for thresholding and cluster division combined. All other analysis steps took less than 1 sec.

Figure 5A shows an original small image of prostate tissue, the result from thresholding the image (Fig. 5B), and the filtered versions are shown in Figure 5C and D. The results from applying thresholding and cluster division to the images in Figure 5A, C, and 5D are shown in Figure 5E, F, and G, respectively, and the result from the full image analysis is shown in Figure 5H. Figure 5B shows that thresholding alone correctly detected 12 out of 18 nuclei (the nuclei without arrows). Five incorrect nuclei (arrows) were appearing to touch each other and therefore were not detected as individual regions. The threshold intensity was too high for proper segmentation of the sixth incorrect nucleus (arrowhead). Figure 5E shows that thresholding of the original image followed by cluster detection and division, but not using the decision algorithm to combine the results with those from the filtered versions, correctly detected 14 out of 18 nuclei. Two nuclei (arrows) were incorrectly divided and two (marked "M") were missed. The missed nuclei were in a cluster that was not divided and was subsequently rejected for being too irregular in shape. Application of the cluster division to the low-pass filtered version (Fig. 5C) gave similar results (compare Fig. 5F to 5E), except one nucleus incorrectly divided in Figure 5E was correctly detected. Figure 5G shows the results from applying cluster division to the high-pass filtered version (Fig. 5D). All nuclei except two (arrows) were correctly detected. Figure 5E, F, and G together show that all nuclei were correctly segmented from at least one of the input images. Thus, when the decision algorithm was applied to these results, it was able to select a combination of regions that resulted in all 18 nuclei being correctly detected (Fig. 5H). Finally, Figure 5I shows the subset of 14 out of 18 correctly detected nuclei that produced essentially the same segmentation from the original image and both filtered versions; these 14 nuclei were considered correctly detected.

Figure 6 shows a 1,280 × 1,024 image of a prostate section (Fig. 6A), the detected regions (Fig. 6B), and the edges of the regions (Fig. 6C). Figure 6C is included to show the boundaries of the regions that are not visible in Figure 6B. The image shows 96 isolated and 31 clustered epithelial nuclei, of which 95 (99%) and 29 (94%), respectively, were correctly detected. In addition, one detected region was not considered to be a nucleus. Hence, the overall performance, calculated using expression (2), was 97%. The right quarter of Figure 6A contains stromal cells. These were not efficiently detected, because the parameters in the algorithms were not set to appropriate values for their detection. The group of regions in the top left corner (marked as "ART" in Fig. 6B) are artifacts. They arose

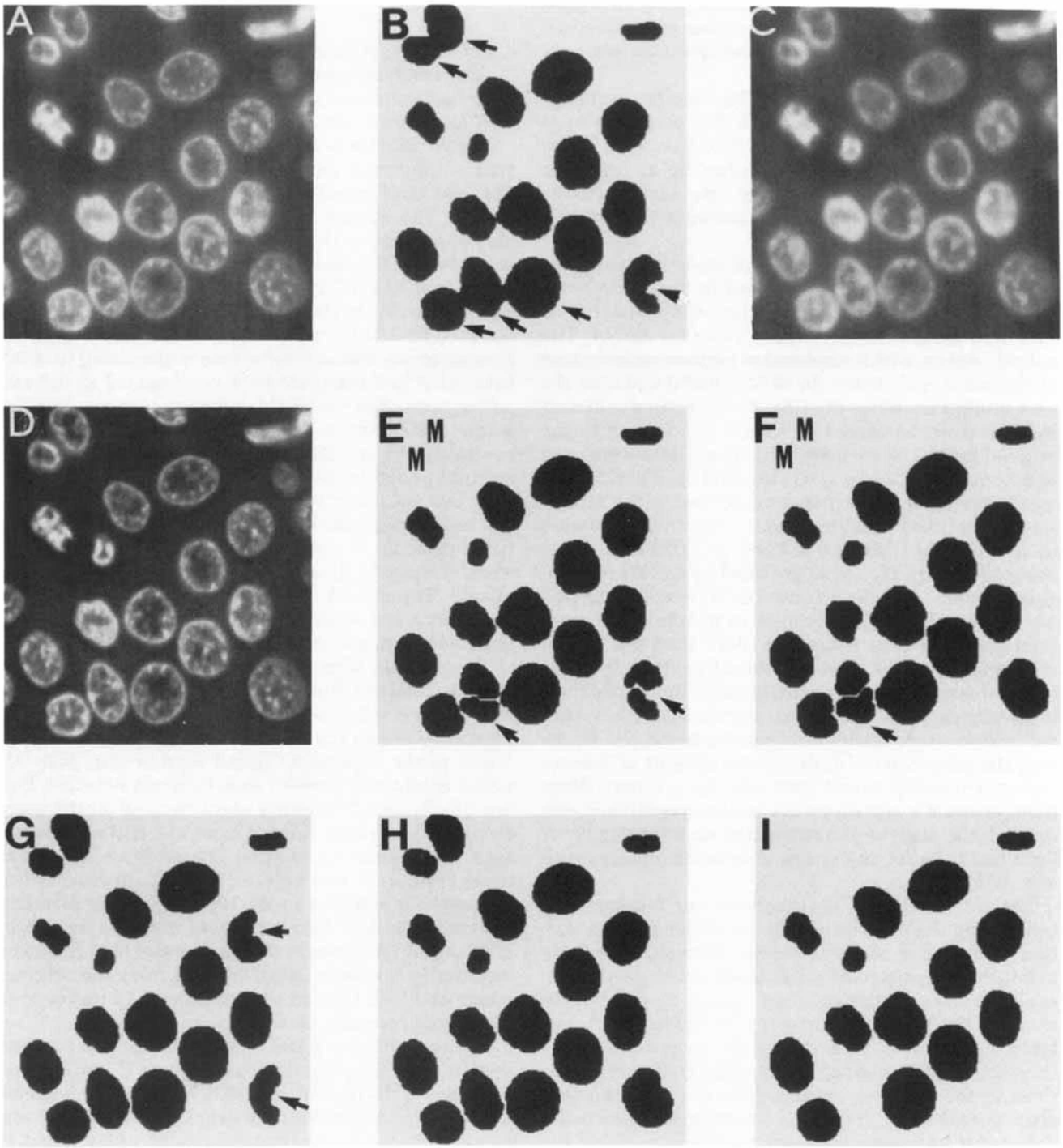

FIG. 5. Analysis of a 256 × 256 image of prostate tissue. **A:** The original image showing 18 nuclei (not counting those nuclei on the edges of the image, which were rejected by the analysis). **B:** Result from applying image thresholding to image (A). The five arrows and arrowhead indicate incorrectly segmented nuclei. **C:** Low-pass filtered version of image (A). **D:** High-pass filtered version of image (A). **E, F, G:** The results from applying thresholding and cluster division to images (A), (C), and (D), respectively. "M" indicates the approximate locations of missed nuclei. **H:** Result from applying the full image analysis to image (A). **I:** regions representing nuclei that produced essentially the same segmentation from (A), (C), and (D).

because the small image for that section contained only background and noise intensities and consequently the threshold intensities were calculated to approximately equal the background intensity level. However, these regions can be easily recognized and eliminated because their pixel intensities equal background intensi-

ties. In total, 296 isolated and 174 clustered epithelial prostate nuclei from the 7 acquired 1,280 × 1,024 images were analyzed, of which 291 (98%) and 166 (95%) were correctly detected. In addition, seven regions considered to be nuclei by the algorithm were not considered to be nuclei by visual examination. Hence, overall performance for detecting nuclei in prostate sections was 96%.

Figure 7 shows a 1,280 × 1,024 image of breast tissue, the detected regions, and the edges of the regions. Only the third of this image that contained most of the clustered nuclei was analyzed. This third contained 37 isolated and 97 clustered epithelial nuclei, of which 37 (100%) and 88 (91%) were correctly detected. In addition, three detected regions were not considered nuclei. Hence, the overall performance was 91%. However, this result is for images deliberately selected because they contained clustered nuclei, therefore the overall performance for typical breast section images should be higher.

The breast image was also used to assess the performance of the major components of the analysis procedure and Table 1 shows the results. The results show a significant improvement when going from only thresholding (performance = 28%), to cluster division (68%) and to the full analysis (91%). Furthermore, by selecting only regions that had essentially the same segmentation from the original image and both filtered versions, 97% of the detected regions were correct.

DISCUSSION

We have developed image analysis algorithms that correctly detect at least 90% of individual fluorescent nuclei in specimens containing large proportions of clustered nuclei. To our knowledge, this is the first report of an algorithm capable of correctly detecting such a high percentage of clustered nuclei in these types of specimens. Consequently, the analysis described here should increase the utility of IC for biological and clinical applications.

We believe the reasons for our high rate of detection were because: (1) The Hoechst staining enabled highly reliable segmentation (by intensity thresholding) of the images into regions corresponding to background and nuclei. (2) The cluster division algorithm exploited the fact that the dividing paths were most likely to cross clusters at necks and be at pixels with high gradients. In other words, the algorithm simultaneously utilized both morphological and intensity information to find the dividing lines across clusters. (3) A few pixels with aberrant intensities (mainly due to variations in the DNA concentration within nuclei) would not significantly disrupt the true path, because the determination of the dividing paths was based on a gradient parameter averaged over many pixels (≈30 pixels). (4) Filtering the images, followed by separately analyzing the original image and filtered versions and then selecting the regions closest to the expected shape of nuclei, made the analysis robust by providing another

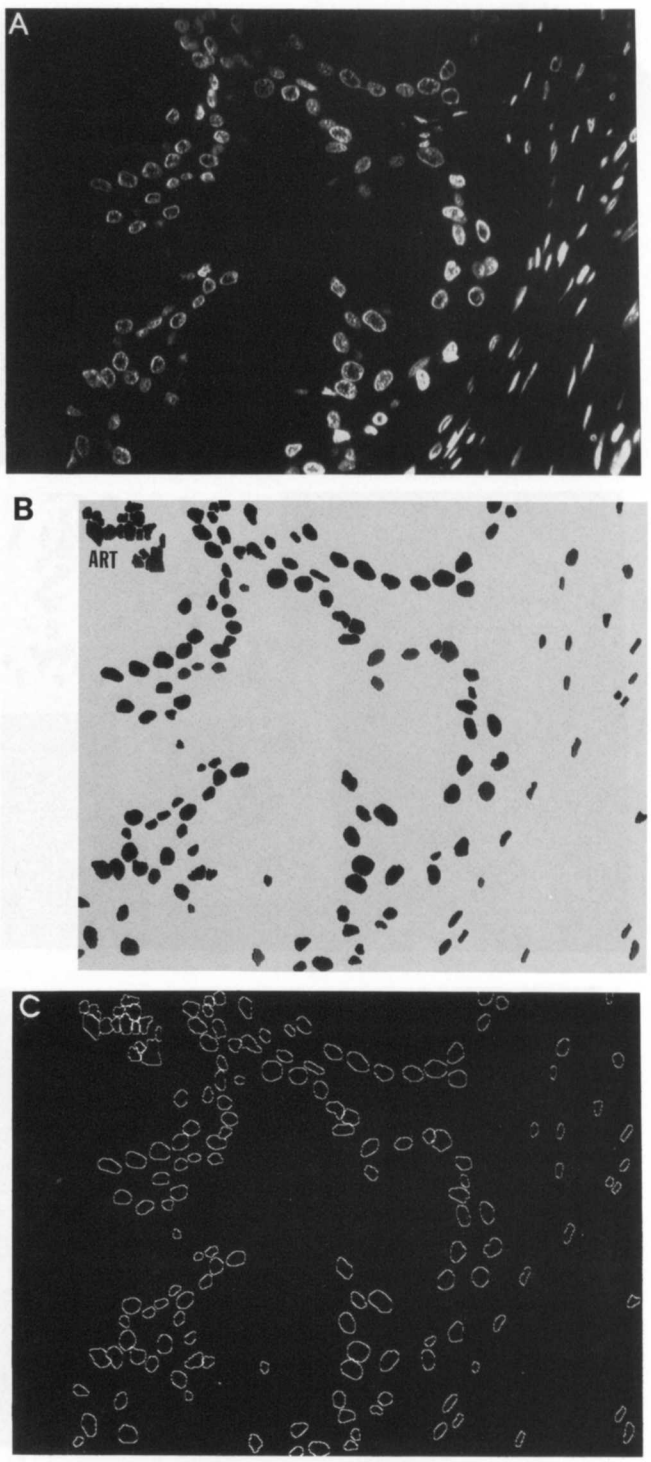

FIG. 6. Analysis of an image of prostate tissue. The right quarter of the figure contains stromal cells. These were not efficiently detected, because the parameters in the algorithms were not set to appropriate values for their detection. **A:** Original 1280 × 1024 image. **B:** Result from the full analysis. "ART" is a group of detected regions that were not nuclei. **C:** The edges of the detected regions, which are included to show the boundaries of regions not visible in (B). (*AREA*, m_A, σ_A, m_S, σ_S) = (1,000, 656, 233, 12.4, 1.6) pixels.

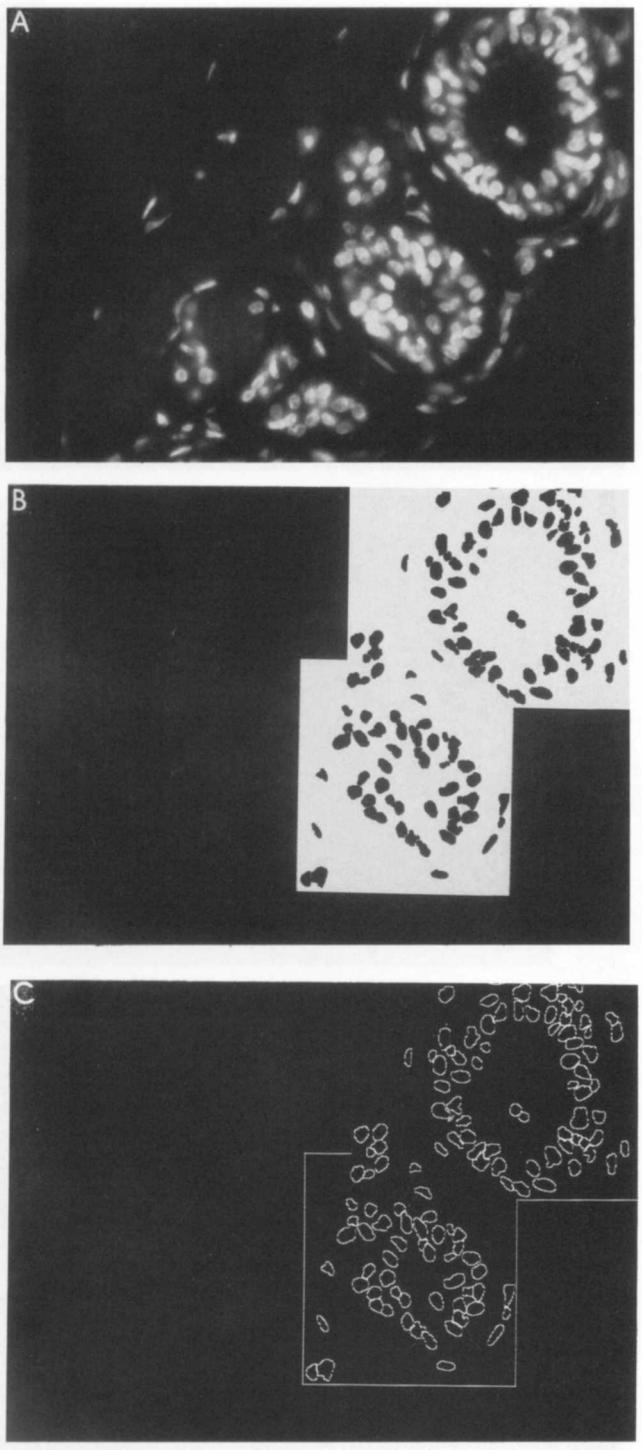

FIG. 7. Analysis of an image of breast tissue. **A:** The original 1,280 × 1,024 image. **B:** Result from the full analysis of the third of the image containing most of the clustered nuclei. **C:** The edges of the detected regions. (*AREA*, m_A, σ_A, m_S, σ_S) = (860, 490, 150, 13.4, 3.3) pixels.

chance to obtain the correct result when cluster division failed on the original image.

The manual determination of the parameters, *AREA*, m_A, σ_A, m_S, and σ_S could be considered a drawback for practical, automated application. However, these parameters need only be known approximately and once they are known for a particular specimen type, subsequent analyses of the same types will be completely automatic.

Table 1
Results From Assessing the Major Components of the Analysis Procedure When Applied to the Breast Section Image

Image analysis procedure	Ratio of correctly detected nuclei to visible nuclei
Only thresholding the original image	37/134 = 28%
Thresholding and applying cluster division to the original image	91/134 = 68%
Full analysis	(125–3[a])/134 = 91%
Selecting only objects that had essentially the same segmentation from the original image and both filtered versions	67/69 = 97%[b]

[a]The three regions not considered to represent nuclei.
[b]Sixty-nine out of 134 of the nuclei were detected.

The potential for further improvements in the analysis exist, for example, using expert system guided scene segmentation (3), applying more filterings and thus extending the approach to multiresolution analysis (12,18), or using unsupervised segmentation algorithms which also estimate the model parameters (43). Furthermore, it would be possible to use an edge relocation algorithm to refine the nuclear contours (27). We could have further tested our approach using thicker specimens (≈50 μm) where greater overlap of cells is expected. However, we believe that the best possible results for such specimens would be achieved by using 3D microscopy followed by 3D image analysis (8), instead of our 2D approach. In addition, the use of thicker specimens together with 3D analysis has the advantages that it would permit the analysis of whole nuclei (34) and avoid the limitations of conventional two-dimensional (2D) microscopy, which are that 2D images are projections through inherently 3D structures and contain out of focus haze (39). At this juncture, it should be pointed out that the algorithms described herein can be extended for 3D application and that automatic segmentation procedures are virtually essential for 3D analysis. This is because manual segmentation would require the definition of the entire surface of structures, and not just the edges as in 2D analysis.

The results produced by the algorithms described herein either detect every nucleus or detect a subset of nuclei at a higher level of reliability. Detecting all nuclei is suitable for applications such as quantifying the distribution of the epithelial nuclei surrounding ducts (6). Detecting a subset of nuclei reliably is suitable for determining the proportion of nuclei expressing a particular intranuclear signal, i.e., the counting of FISH

labeled gene sequences in the interphase nuclei of cancer specimens (28).

The results presented herein show that a high proportion (more than 90%) of fluorescence labeled nuclei, including nuclei appearing to touch and overlap, can be automatically and correctly detected using fluorescence digital image-based cytometry (IC). The core of the IC is algorithms that locate dividing paths between clustered nuclei and select, from the segmentations of the original image and filtered versions of the same nuclei, the correct regions representing nuclei. The algorithms we have developed will lead to the more convenient analysis of a greater proportion of nuclei in intact specimens. This, in turn, will lead to more precise diagnosis of clinical specimens and improved understanding of cellular mechanisms.

ACKNOWLEDGMENTS

We gratefully acknowledge Mr. J. McNeil for preparing the tissue sections and Dr. G. Gordon, Mr. P. Wodnicki, and Mr. M. McAuliffe for their expert review of the manuscript.

LITERATURE CITED

1. Ahrens P, Schleicher A, Zilles K, Werner L: Image analysis of Nissl-stained neuronal perikarya in the primary visual cortex of the rat: Automatic detection and segmentation of neuronal profiles with nuclei and nucleoli. J Microsc 157:349–365, 1990.
2. Bartels PH, Weber JE, Paplanus SH, Graham AR: Detection of diagnostic clues in statistical histometry. Anal Quant Cytol Histol 9:355–368, 1987.
3. Bartels PH, Bibbo M, Graham A, Paplanus S, Shoemaker RL, Thompson D: Image understanding system for histopathology. Anal Cell Pathol 1:195–214, 1989.
4. Bartels PH, Thompson D, Bartels HG, Shoemaker R: Machine vision system for diagnostic histopathology. Pathol Res Pract 185: 635–646, 1989.
5. Bennett HS, Wyrick AD, Lee SW, McNeil JH: Science and art in preparing tissues embedded in plastic for light microscopy, with special reference to glycol methacrylate, glass knives and simple stains. Stain Tech 51:71–97, 1976.
6. Bibbo M, Kim DH, di Loreto C, Dytch HE, Galera-Davidson H, Thompson D, Richards DL, Bartels HG, Bartels PH: Tissue architectural features for the grading of prostatic carcinoma. Anal Quant Cytol Histol 12:229–236, 1990.
7. Bins M, Takens F: A method to estimate the DNA content of whole nuclei from measurements made on thin tissue sections. Cytometry 6:234–237, 1985.
8. Boon ME, Kok LP, Sutedja G, Dutrieux RP: Confocal sectioning of thick, otherwise undiagnosable cell groupings in cervical smears. Acta Cytol 37:40–48, 1993.
9. Claeys A, Van Den Branden C, Roels F: Automated measurements on cell nuclei in tissue sections: Validation procedures. Anal Quant Cytol Histol 10:276–284, 1988.
10. DiGuiseppi J, Inman R, Ishihara A, Jacobson K, Herman B: Applications of digitized fluorescence microscopy to problems in cell biology. BioTechniques 3:393–403, 1985.
11. Garbay C, Chassery J-M, Brugal G: An iterative region-growing process for cell image segmentation based on local color similarity and global shape criteria. Anal Quant Cytol Histol 8:25–34, 1986.
12. Gauch JM, Pizer SM: Multiresolution analysis of ridges and valleys in grey-scale images. IEEE Trans Patt Anal Mach Int 15: 635–646, 1993.
13. Gonzalez RC, Wintz P: Digital Image Processing. Addison-Wesley Publishing Co., Reading, 1987, pp 161–162.
14. Gonzalez RC, Wintz P: Digital Image Processing. Addison-Wesley Publishing Co., Reading, 1987, p 337.
15. Gonzalez RC, Wintz P: Digital Image Processing. Addison-Wesley Publishing Co., Reading, 1987, pp 176–179.
16. Gonzalez RC, Wintz P: Digital Image Processing. Addison-Wesley Publishing Co., Reading, 1987, pp 398–402.
17. Gonzalez RC, Wintz P: Digital Image Processing. Addison-Wesley Publishing Co., Reading, 1987, p 399.
18. Griffin LD, Colchester ACF, Robinson GP: Scale and segmentation of grey-level images using maximum gradient paths. In: Lecture Notes in Computer Science, Colchester ACF, and Hawkes DJ (eds). 12th International Conference IPMI, Wye, England, 1991, pp 256–272.
19. Henderson BE, Ross RK, Pike MC: Toward the primary prevention of cancer. Science 254:1131–1138, 1991.
20. King EB, Chew KL, Duarte L, Hom JD, Mayall BH, Miller TR, Petrakis NL: Image cytometric classification of premalignant breast disease in fine needle aspirates. Cancer 62:114–124, 1988.
21. Liang XH, Volkmann M, Klein R, Herman B, Lockett SJ: Colocalization of the tumor-suppressor protein p53 and human papillomavirus E6 protein in human cervical carcinoma cell lines. Oncogene 8:2645–2652, 1993.
22. Liedtke CE, Gahm T, Kappei F, Aeikens B: Segmentation of microscopic cell scenes. Anal Quant Cytol Histol 9:197–211, 1987.
23. Lockett SJ, O'Rand M, Rinehart C, Kaufman D, Jacobson K, Herman B: Automated measurement of DNA ploidy using fluorescence microscopy. In: Optical Microscopy in Biology, Herman B, and Jacobson K (eds). Alan R. Liss, Inc., New York, 1990, pp 603–613.
24. Lockett SJ, O'Rand M, Rinehart CA, Kaufman DG, Herman B, Jacobson K: Automated fluorescence image cytometry: DNA quantification and detection of chlamydial infections. Anal Quant Cytol Histol 13:27–44, 1991.
25. Lockett SJ, Jacobson K, Herman B: Quantitative precision of an automated, fluorescence-based image cytometer. Anal Quant Cytol Histol 14:187–202, 1992.
26. MacAulay C, Palcic B: A comparison of some quick and simple threshold selection methods for stained cells. Anal Quant Cytol Histol 10:134–138, 1988.
27. MacAulay C, Palcic B: An edge relocation segmentation algorithm. Anal Quant Cytol Histol 12:165–171, 1990.
28. Matsumura K, Kallioniemi A, Kallioniemi O, Chen L, Smith HS, Pinkel D, Gray J, Waldman FM: Deletion of chromosome 17p loci in breast cancer cells detected by fluorescence in situ hybridization. Cancer Res 52:3474–3477, 1992.
29. Mellin W: Cytopathology in tumor pathology: A critical review of methods and applications, and some results of DNA analysis. Pathol Res Pract 186:37–62, 1990.
30. Meyer F: Mathematical morphology: From two dimensions to three dimensions. J Microsc 165:5–28, 1992.
31. Poon SSS, Ward RK, Palcic B: Automated image detection and segmentation in blood smears. Cytometry 13:766–774, 1992.
32. Press WH, Flannery BP, Teukolsky SA, Vetterling WT: Numerical recipes in C. Cambridge University Press, Cambridge, 1990, p 519.
33. Preston K: Tissue section analysis: Feature selection and image processing. Patt Reg 13:17–36, 1981.
34. Rigaut JP, Vassy J, Herlin P, Duigou F, Masson E, Briane D, Foucrier J, Carvajal-Gonzalez S, Downs AM, Mandard A-M: Three-dimensional DNA image cytometry by confocal scanning laser microscopy in thick tissue blocks. Cytometry 12:511–524, 1991.
35. Rutovitz D: Data structures for operations on digital images. In: Pictorial Pattern Recognition. Thompson, Washington DC, 1968, pp 105–133.
36. Samarabandu JK, Acharya R, Edirisinghe CD, Cheng PC, Kim H, Lin TH, Summers RG, Musial CE: Analysis of multi-dimensional confocal images. Proc SPIE 1450:296–322, 1991.
37. Serra J: Image Analysis and Mathematical Morphology. Academic Press, New York, 1982.
38. Siadat-Pajouh M, Periasamy A, Ayscue AH, Moscicki AB, Palefsky JB, Walton L, DeMars LR, Power JD, Herman B, Lockett SJ:

Detection of human papillomavirus type 16/18 DNA in cervicovaginal cells by fluorescence based in situ hybridization and automated image cytometry. Cytometry 15:245–257, 1993.
39. Stelzer EHK, Wacker I, De Mey JR: Confocal fluorescence microscopy in modern cell biology. Semin Cell Biol 2:145–52, 1991.
40. Tanke HJ: Does light microscopy have a future? J Microsc 155: 405–418, 1989.
41. Thomas ADH, Davies T, Luxmoore AR: The Hough transform for locating cell nuclei. Anal Quant Cytol Histol 14:347–353, 1992.
42. Wolf G: Use of global information and a priori knowledge for segmentation of objects: Algorithms and applications. Proc SPIE 1660:397–408, 1992.
43. Won CS, Derin H: Unsupervised segmentation of noisy and textured images using Markov random fields. CVGIP: Graph Mod Image Proc 54:308–328, 1992.